Available online at www.sciencedirect.com
ScienceDirect
Trans. Nonferrous Met. Soc. China 32(2022) 778−789
Transactions of Nonferrous Metals Society of China
www.tnmsc.cn

Microstructure, mechanical properties and corrosion behavior of commercial 7N01 alloys

Pei-hao ZHAO[1], Xiao-lan WU[1], Yang LIU[1], Kun-yuan GAO[1], Sheng-ping WEN[1], Wu WEI[1], Li RONG[1], Hui HUANG[1], Hong WU[2], De-jing ZHOU[3], Qian ZHANG[4], Zuo-ren NIE[1]

1. Faculty of Materials and Manufacturing, Beijing University of Technology, Beijing 100124, China;
2. State Key Laboratory of Powder Metallurgy, Central South University, Changsha 410083, China;
3. Jiangsu Key Laboratory for Clad Materials, Yin Bang Clad Material Co., Ltd., Wuxi 214145, China;
4. Metal & Chemistry Institute, China Academy of Railway Sciences Corporation Limited, Beijing 100081, China

Received 12 April 2021; accepted 30 October 2021

Abstract: The effect of grain morphology and precipitates on mechanical properties and corrosion behavior of two commercial 7N01 alloys was studied using transmission electron microscopy (TEM) and scanning electron microscopy (SEM) equipped with electron backscatter diffraction (EBSD). Results showed that the recrystallization degree of the outer surface of 7N01-I alloy was lower than that of 7N01-II alloy. The main strengthening precipitates of two alloys were mainly η' phases. The grain boundary precipitates (GBPs) of 7N01-I alloy distributed discontinuously, while those of 7N01-II alloy distributed continuously. The strength of two 7N01 alloys was similar, but the maximum corrosion depth of 7N01-I alloy was less than that of 7N01-II alloy, because the discontinuous GBPs and the lower recrystallization degree of outer surface of 7N01-I alloy were favorable for improving corrosion behavior. Different models of strengthening mechanism were discussed, and the corrosion behavior was correlated with microstructure.
Key words: 7N01 alloys; microstructure; mechanical properties; corrosion behavior

1 Introduction

Heat-treatable Al−Zn−Mg alloys were widely used as structural parts in high-speed rails due to their sufficient strength and excellent formability [1,2]. The grain size, recrystallization degree and precipitates characteristics directly determined the properties of alloys. With increasing the recrystallization degree, the yield strength of Al−Zn−Mg alloys usually decreased. Improving hot deformation process and reducing recrystallization degree had become one of main methods to enhance the strength. It was found that inhibiting recrystallization was conductive to improving the yield strength and tensile strength of alloys [3−7]. The size and distribution of precipitates were also important factors affecting mechanical strength. The metastable $MgZn_2$ phase (η' phase) was referred to as the main strengthening phase. The η' phase has a hexagonal structure with a=0.496 nm and c=1.402 nm and is semi-coherent with the matrix. The orientation relationship between η' phase and α(Al) was $(0001)_{\eta'}//(111)_{Al}$ and $[10\bar{1}0]_{\eta'}//[110]_{Al}$. The stable $MgZn_2$ phase (η phase) which has a hexagonal structure with a=0.515 nm and c=0.848 nm was non-coherent with the matrix and showed eleven orientation relationships with the matrix [8−11].

However, mechanical properties and corrosion resistance of Al−Zn−Mg alloys could not be optimized at the same time. Especially under peak

Corresponding author: Xiao-lan WU, Tel: +86-18600913802, E-mail: xiaolan.wu@bjut.edu.cn;
Zuo-ren NIE, Tel: +86-10-67391536, E-mail: zrnie@bjut.edu.cn
DOI: 10.1016/S1003-6326(22)65832-1

aging condition, the corrosion behavior of Al−Zn−Mg alloys deteriorated with the increase of strength [12−16]. The intergranular corrosion (IGC) and exfoliation corrosion (EXCO) of alloys were caused by potential difference between the grain boundary precipitates (GBPs) and precipitation free zone (PFZ). The anodic dissolution was the main mechanism of corrosion [12,17,18].

Many works have been done to improve corrosion behavior of Al−Zn−Mg alloys. The proper heat treatment played an important role in improving microstructure and corrosion resistance of alloys. The morphology of GBPs and the width of PFZ could be controlled by changing the heat treatment process [19]. GBPs were easy to be corroded preferentially as the anode because of the potential difference between GBPs and the matrix. The discontinuous GBPs helped to reduce the number of corrosion sites and improved corrosion resistance [20−22]. The PFZ formation in the aluminum alloy caused reduction in the strength (about 100 MPa) [23]. The maximum shear stresses always occurred in the PFZ which were at an angle of 45° from the applied stress. The PFZ was deformed preferentially under the loading and had a significant effect on properties [24]. The ultimate tensile strength and yield strength decreased with the increase of the width of the PFZ [25]. The wider PFZ, which was relative softer, was conducive to crack propagation when the crack initiated. Therefore, it was found that improving corrosion resistance mainly depended on the transformation of GBPs and PFZ.

Two extruded commercial 7N01 alloys have been investigated in this work. The microstructure was investigated by transmission electron microscopy (TEM) and scanning electron microscopy (SEM) equipped with electron backscatter diffraction (EBSD). The mechanical properties and corrosion behavior were tested. And the correlation among microstructure, mechanical properties and corrosion behavior was analyzed.

2 Experimental

Two commercial 7N01 alloys were obtained from two different companies for study. The commercial profile is shown in Fig. 1. The compositions of two 7N01 alloys are given in Table 1. In order to investigate the microstructures of two 7N01 alloys, samples were taken in transverse section and longitudinal section from five locations which were inner surface, a quarter-thickness from the inner surface, center, a quarter-thickness from the outer surfaces and outer surface.

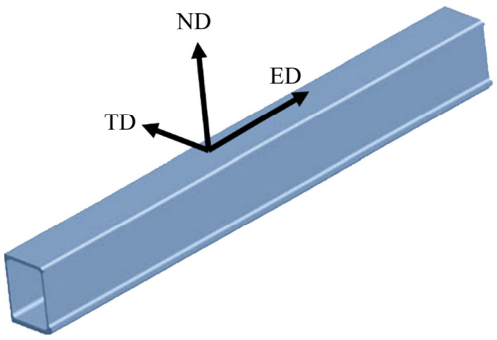

Fig. 1 Schematic diagram of extruded commercial 7N01 alloys (ED−Extrusion direction; ND−Normal direction; TD−Transverse direction)

The microstructure was analyzed by a FEI Helios 600i SEM equipped with EBSD operating at 20 kV. The samples for EBSD analysis were electropolished with a solution of 85% ethanol, 5% perchloric acid and 10% high purity water at 20 V for 15 s. The grain size and aspect ratio were analyzed through HKL Channel 5. The samples prepared by electropolishing in the same processing with the EBSD samples, were used to obtain high resolution images of coarse secondary precipitates using SEM. The size of precipitates was measured by Nano measure software and averaged from more than 300 measured precipitates. The precipitates were analyzed by JEM 2100F TEM operating at

Table 1 Compositions of 7N01 alloys (wt.%)

Alloy	Zn	Mg	Mn	Cu	Cr	Ti	Zr	Fe	Si	Al
Nominal	4.0−5.0	1.0−2.0	0.20−0.70	0.20	0.30	0.20	0.25	0.35	0.30	Bal.
7N01-I	4.12	1.07	0.39	0.17	0.22	0.05	0.13	0.17	0.06	Bal.
7N01-II	4.27	0.93	0.30	0.05	0.22	0.06	0.14	0.12	0.12	Bal.

200 kV. TEM samples were taken on transverse section. The samples were ground to a thickness less than 100 μm, and then punched into 3 mm discs. Final double-jet polishing was performed with an electrolyte solution of 20% nitric acid and 80% methanol at the voltage of 15−25 V (DC) and at the temperature from −25 to −30 °C.

The Vickers hardness of these samples was tested using HXD−1000TM/LCD hardness tester with 0.98 N for 10 s. The average value of eight measurements was calculated with standard deviations. Mechanical properties of two alloys were tested according to the standard of GB/T 228.1—2010. The IGC test was carried out in the solution of 3 g NaCl + 1 mL HCl and 100 mL H_2O at (35±2) °C in the water bath for 6 h followed by the standard of GB/T 7998—2005 [26]. The EXCO test was executed in the solution containing 0.5 mol/L KNO_3, 0.1 mol/L HNO_3 and 4 mol/L NaCl at (25±3) °C in water bath for 48 h followed by standard of GB/T 22639—2008 [27]. Three parallel samples were used for these tests.

3 Results and discussion

3.1 Microstructure characterization

Figure 2 shows EBSD maps of two 7N01 alloys in the transverse section and longitudinal section. Coarse grains were found in the inner surface and outer surface of two 7N01 alloys and equiaxed grains were close to the coarse grain. Disk-shaped grains and equiaxed grains co-existed in the center and quarter-thickness from surfaces, but the width of the disk-shaped grains in the center was larger than that in quarter-thickness from surfaces. Except for the outer surface, the grain morphology of 7N01-II alloy was similar with that of 7N01-I alloy. The deformed grains and a few equiaxed grains co-existed in the outer surface of 7N01-I alloy, while equiaxed grains uniformly existed in the outer surface of 7N01-II alloy. Moreover, as shown in Fig. 3, the average grain size of 7N01-I alloy was slightly larger than that of 7N01-II alloy.

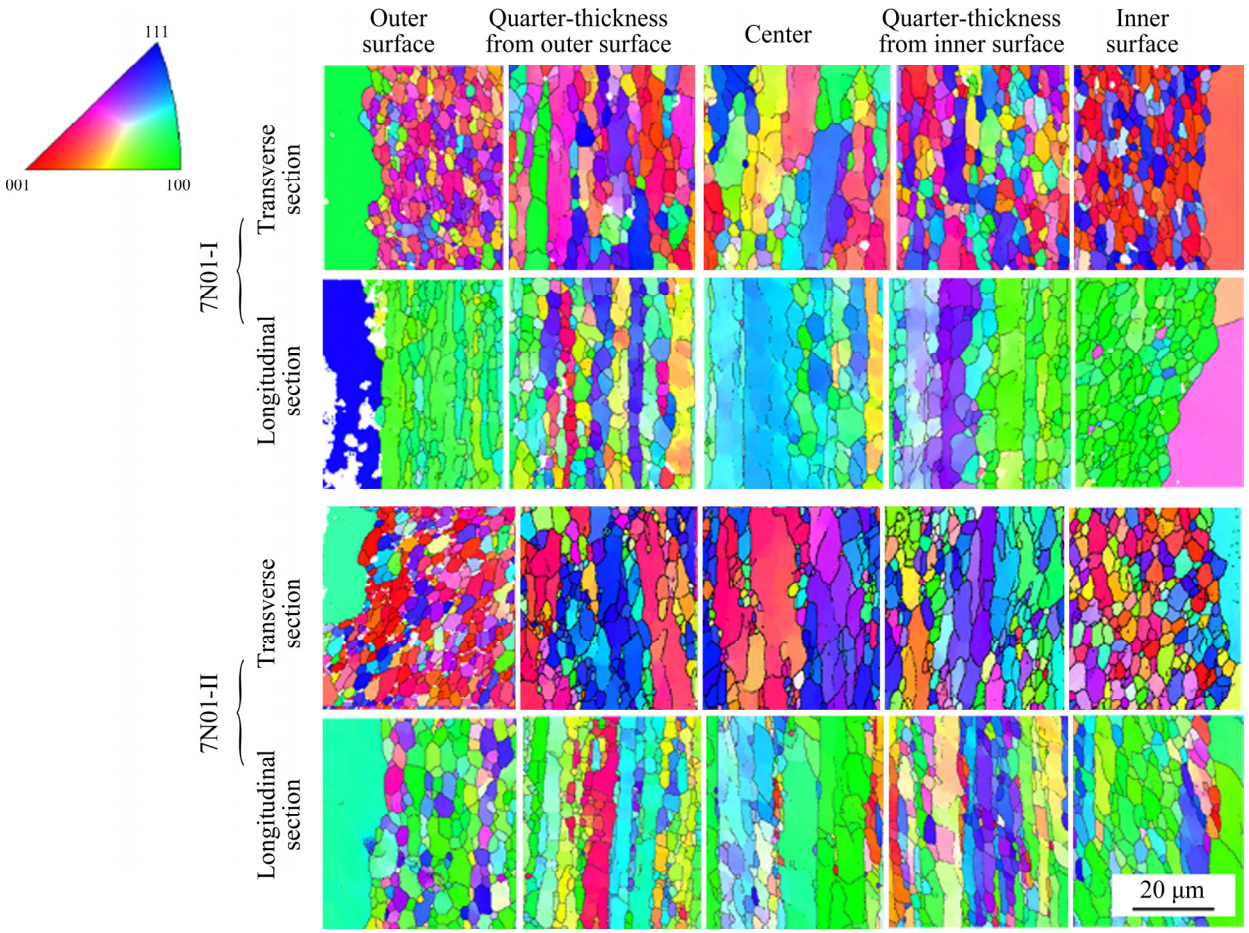

Fig. 2 EBSD maps of two 7N01 alloys in transverse section and longitudinal section

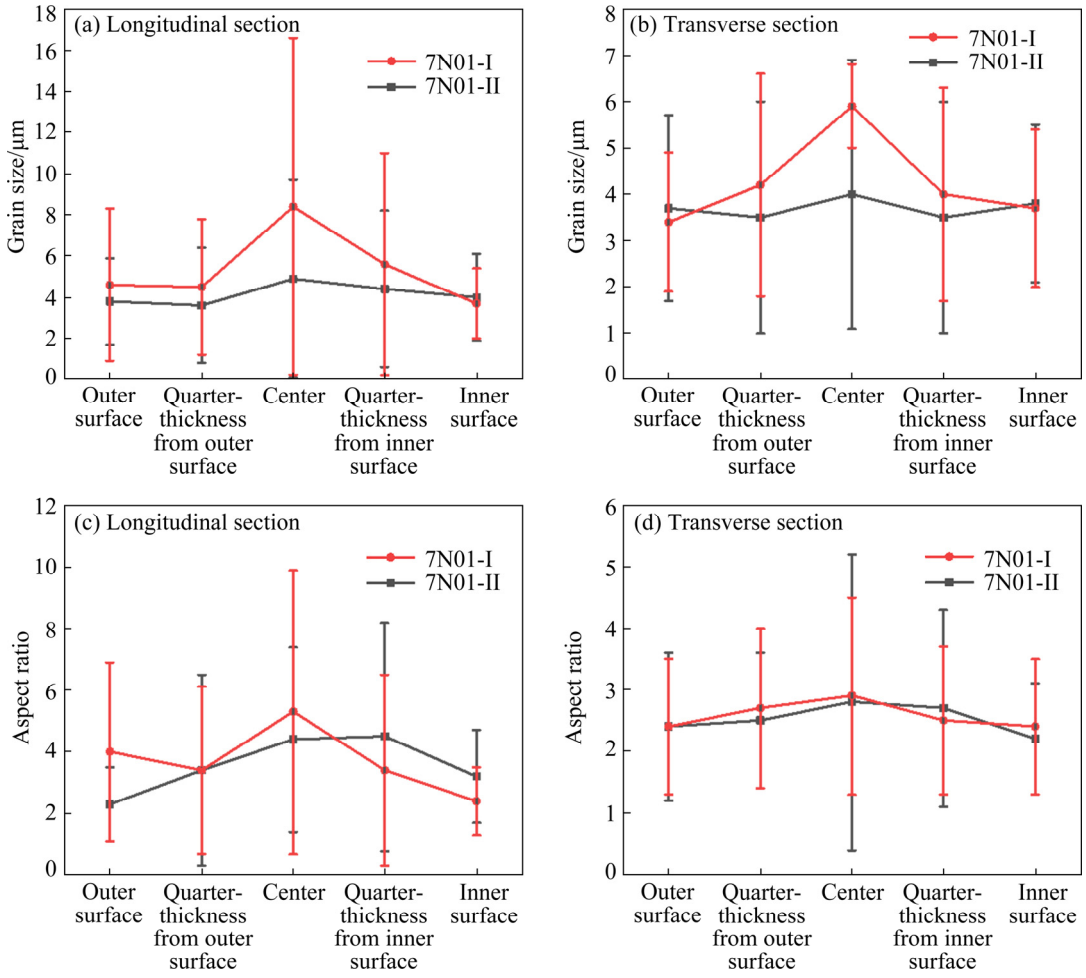

Fig. 3 Grain size (a, b) and aspect ratio (c, d) of different areas of two 7N01 alloys

The recrystallization maps of two 7N01 alloys in transverse section and longitudinal section are shown in Fig. 4. Most of equiaxed grains in the surface were recrystallized grains. The disk-shaped and equiaxed grains in the center and quarter-thickness from the surface were sub-grains and recrystallized grains, respectively. Recrystallization degree of the surface was the highest, followed by that of quarter-thickness from the surface, and that of the center was the lowest. The difference of microstructure between two 7N01 alloys was in grain morphology and recrystallization degree of the outer surface. The recrystallization degree of outer surface of 7N01-I alloy was lower than that of 7N01-II alloy. The sub-grains dominated in the outer surface of 7N01-I alloy while the equiaxed grains was in the majority in the outer surface of 7N01-II alloy.

During the extrusion process, the grains in the surface of alloys were not deformed significantly due to the friction between alloys and the die. Therefore, there was a layer of coarse grains on the surface of two investigated alloys. The equiaxed grains in the surface were recrystallized grains generated after recovery and recrystallization during the hot extrusion. Due to the temperature gradient from the surface to center, the recrystallization degree of the center was much lower than that of the surface. In particular, the recrystallization degree of the outer surface of 7N01-I alloy was smaller than that of 7N01-II alloy, which may be due to the different cooling rates after the extrusion.

3.2 Precipitates

The SEM images of the outer surface of two 7N01 alloys in longitudinal section are shown in Figs. 5(a, b, e, f). The yellow dotted line in Figs. 5(a, e) represents the grain boundary of coarse grain. There were many coarse secondary precipitates with size of 80−200 nm on the surface of 7N01-I alloy. It was obvious that the size of the

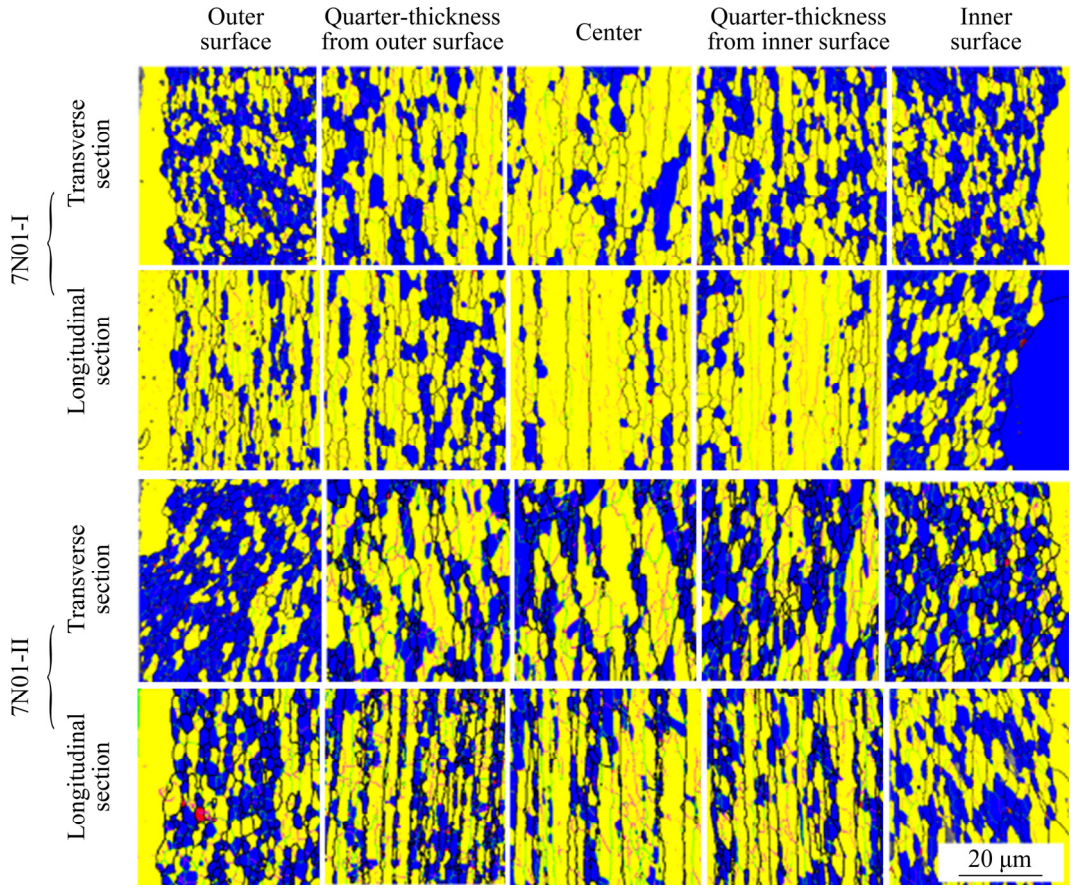

Fig. 4 Recrystallization maps of two 7N01 alloys (Blue represents recrystallized grains and yellow represents sub-grains)

coarse secondary precipitates in surface of 7N01-II alloy was larger than that of 7N01-I alloy. The size of coarse secondary precipitates in the surface of 7N01-II alloy was 120−250 nm. There were many coarse secondary precipitates in the center of two 7N01 alloys, as shown in Figs. 5(c, d, g, h). The sizes of coarse secondary precipitates in the center of 7N01-I alloy and 7N01-II alloy were 60−80 nm and 80−100 nm, respectively. The size of coarse secondary precipitates in the center of two 7N01 alloys was smaller than that in surfaces.

The TEM images of two alloys are presented in Fig. 6. There were many spherical and rod-like fine precipitates in the matrix. The precipitates in the matrix were mainly metastable $MgZn_2$ phase (η') and stable $MgZn_2$ phase (η), which were coherent and semi-coherent with the matrix. As shown in Figs. 6(b, e), η' phases existed uniformly in matrix. The GBPs of 7N01-I alloy distributed discontinuously while the GBPs of 7N01-II alloy distributed continuously. The widths of PFZ in 7N01-I alloy and 7N01-II alloy were 75 nm and 80 nm, respectively. The morphology of GBPs and the width of PFZs had significant effects on corrosion behavior of alloys.

3.3 Mechanical properties

Figure 7 shows the hardness of inner surface, quarter-thickness from inner surface, center, quarter-thickness from outer surface and outer surface of two 7N01 alloys in transverse section and longitudinal section. The hardness of five regions of 7N01-I alloy was all close to HV 121. However, the hardness of five regions of 7N01-II alloy was diverse, and the hardness decreased gradually from center to surface. The hardness values of center and surface were HV 121±2 and HV 115±2, respectively. In the surface of 7N01-II alloy, obvious softening phenomenon existed. The recrystallization degree of the surface of 7N01-II alloy was lower obviously than that of the center, and the fraction of sub-grains in the center was greater than that in the surface. Hence, the hardness of the center was greater than that of the surface.

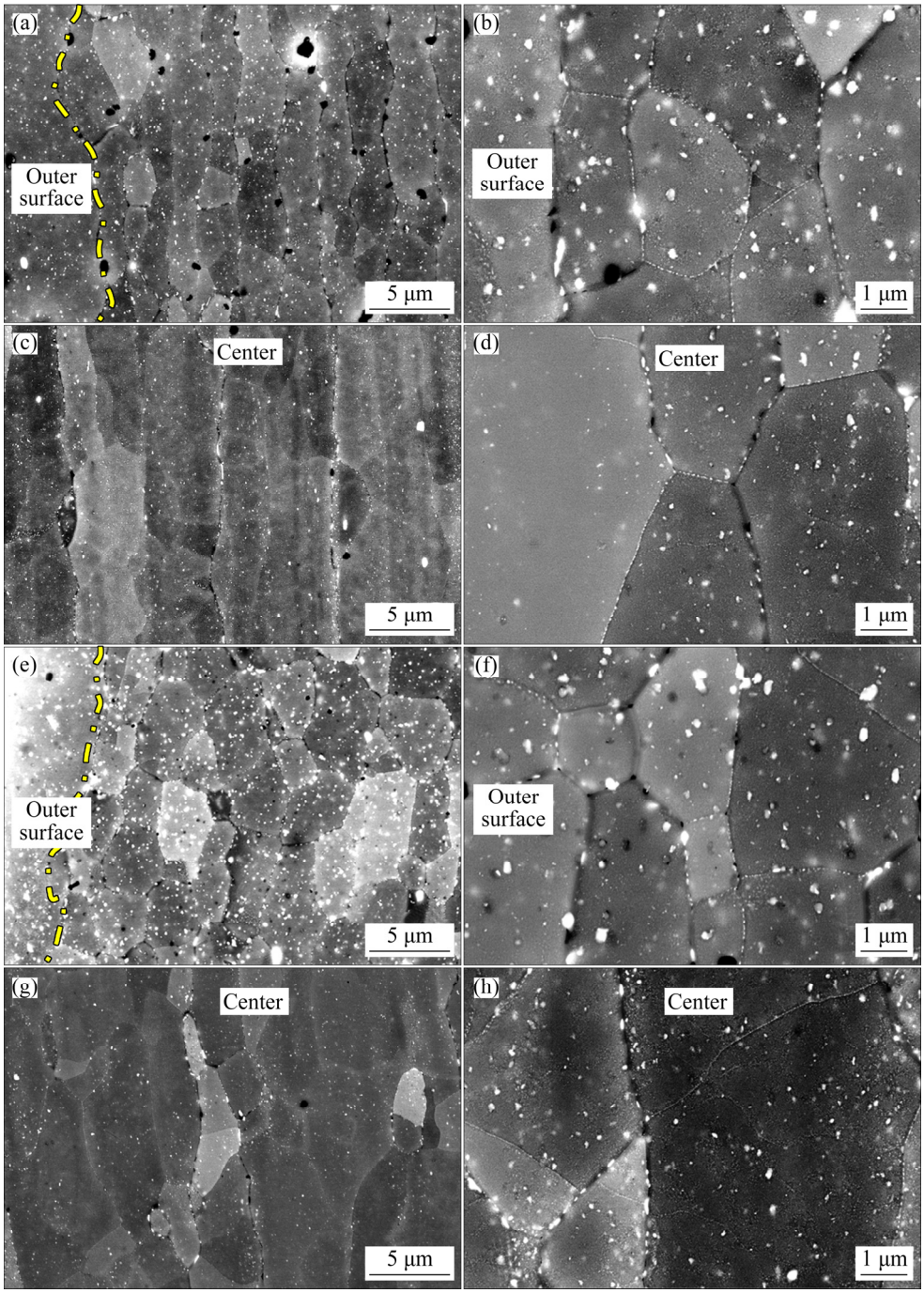

Fig. 5 SEM images of two 7N01 alloys in longitudinal section: (a−d) 7N01-I; (e−h) 7N01-II

Figure 8 presents the yield strength (YS), ultimate tensile strength (UTS), and elongation of two 7N01 alloys. The results showed that the YS, UTS and elongation of two alloys were similar. Although the hardness of the surface of the 7N01-I alloy was lower than that of the center, there was no obvious difference in mechanical strength due to the narrow softening area in the surface. And the distribution characteristic of precipitates was close to each other and there was no difference in mechanical properties.

The strengthening mechanisms of Al−Zn−Mg alloys include grain boundary strengthening, dislocation strengthening, solid solution strengthening and precipitation strengthening. The investigated 7N01 alloys were solution treated after hot deforming, so the contribution of dislocation strengthening could be negligible. Grain boundary strengthening could be described by the Hall–Petch equation as [28]

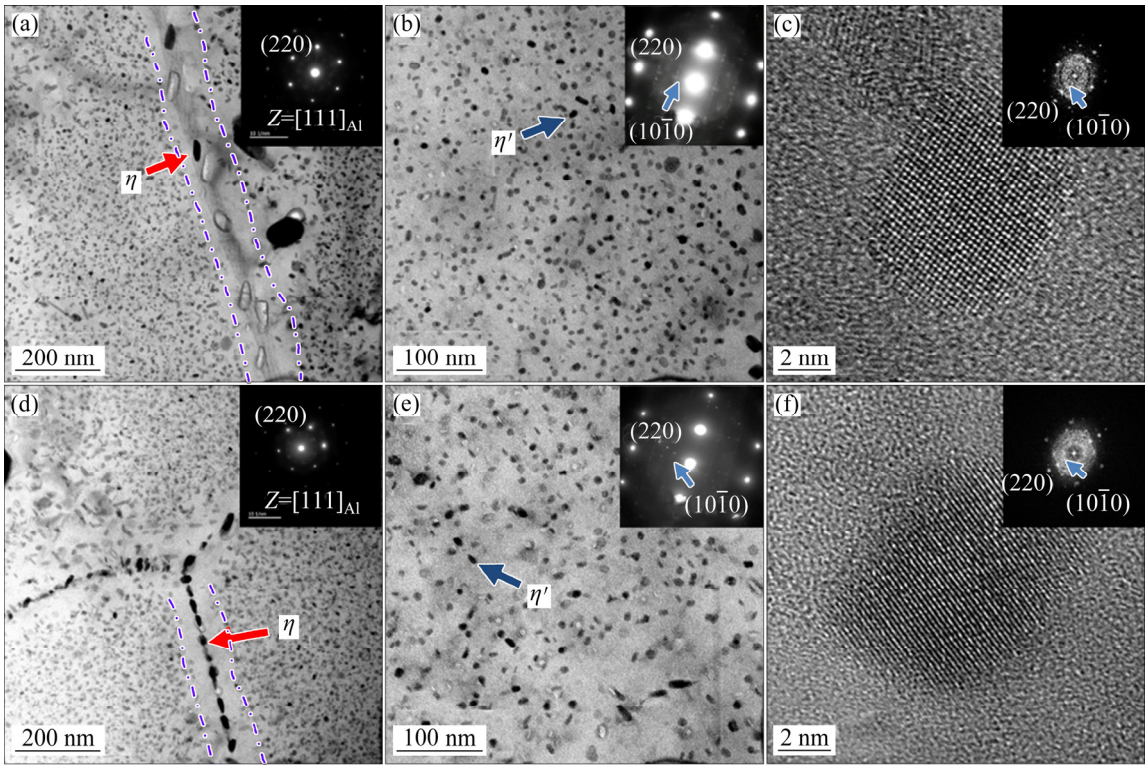

Fig. 6 TEM images of two 7N01 alloys: (a−c) 7N01-I; (d−f) 7N01-II

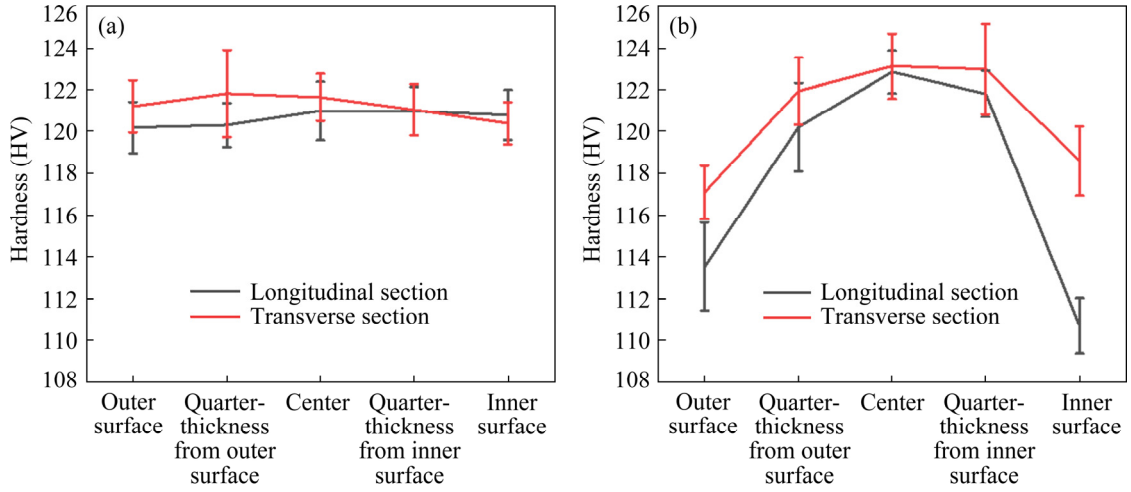

Fig. 7 Hardness of different locations of two 7N01 alloys in transverse section and longitudinal section: (a) 7N01-I; (b) 7N01-II

$$\sigma_{gb}=\sigma_{\alpha}+kd^{-1/2} \quad (1)$$

where σ_{α}(=10 MPa) is the yield strength of pure aluminum [29], k(=0.065 MPa/m$^{1/2}$) is the Hall–Petch constant of pure aluminum [30] and d is the average grain size of alloys. The grain sizes of the center in transvers section of two 7N01 alloys were 5.8 and 4 μm, respectively.

The solute atoms are dissolved in the interstitial or displacement sites of α(Al) matrix. The atoms remained in α(Al) matrix, resulting in the variation of strain field and hindering dislocation motion. The solid solution strengthening was governed by the Mott and Labusch theory [31]:

$$\sigma_{SS}=\Sigma_i\{(A_{SS})_i C_i^{2/3}\} \quad (2)$$

where C_i is molar fraction and A_i is a constant in Mott and Labusch equation. The solid solution strengthening depends on the concentration of solute atoms. Based on other researched alloys with

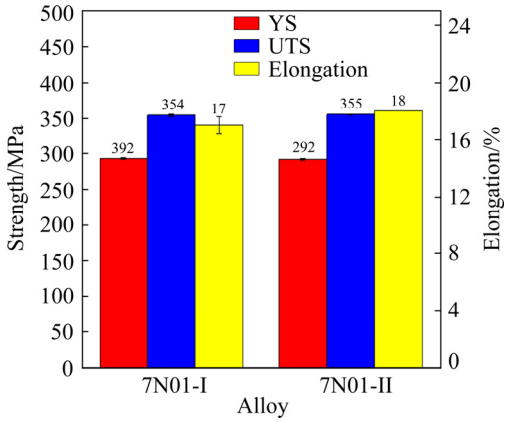

Fig. 8 Tensile properties of two 7N01 alloys

similar composition, the contribution value of solid solution strengthening (σ_{SS}) was about to 59.43 MPa [32].

Precipitation strengthening is the main strengthening mechanism of Al−Zn−Mg alloys. When precipitates were large enough to exceed 2 nm, the dislocation was difficult to cut through the precipitate and bent around the precipitate. The interaction mechanism between the precipitate and dislocation was widely accepted as the Orowan mechanism. The precipitation strengthening could be calculated by using some classical prediction models. The Kocks statistical equation would be chosen to calculate the contribution of precipitation strengthening [29]:

$$\sigma_{ppt}=0.6MGb\left\{\frac{2\sqrt{f_v}}{[D_p/(\pi/4)]}\right\} \quad (3)$$

$$\sigma_y=\sigma_{gb}+\sigma_{SS}+\sigma_{ppt} \quad (4)$$

where M(=2) is the Taylor factor, G(=26 GPa) is the shear modulus of pure aluminum, b(=0.284 nm) is the magnitude of Burgers vector, and f_v and D_p are the volume fraction and average diameter of precipitates, respectively. The diameter, number density and volume fraction of precipitates are listed in Table 2. Equation (4) is used to evaluate the yield strength. And the calculated yield strength and experimental strength are shown in Table 3 and Fig. 9.

It could be seen from Table 3 that the contribution of precipitation strengthening to yield strength was the largest, accounting for 66%. This was consistent with the conclusion that precipitation strengthening was the main strengthening mechanism of Al−Zn−Mg alloys. The

Table 2 Diameter (D_p), number density (N_v) and volume fraction (f_v) of precipitates of two 7N01 alloys

Alloy	D_p/nm	N_v/m^{-3}	f_v/%
7N01-I	7.39	4.44×10^{22}	1.01
7N01-II	8.07	3.41×10^{22}	1.13

Table 3 Experimental yield strength and strength for model prediction of two 7N01 alloys

Alloy	Experimental yield strength/MPa	Strength for model prediction/MPa			
		σ_{gb}	σ_{SS}	σ_{ppt}	σ_y
7N01-I	293±1	37±3	59	189	285±3
7N01-II	292±1	42±11	59	185	286±11

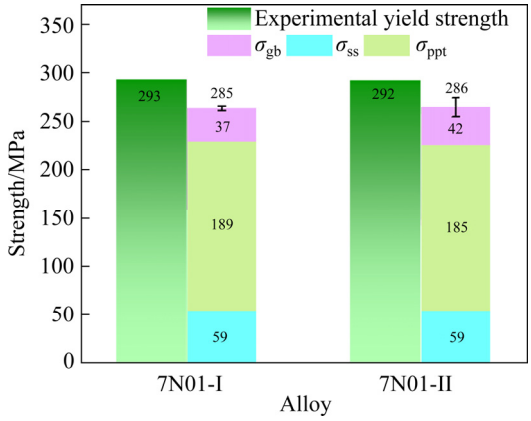

Fig. 9 Comparison of experimental yield strength and strength for model prediction

solid solution strengthening and grain boundary strengthening accounted for 21% and 13%, respectively. After aging treatment, the solubility of solute atoms in the matrix decreased obviously, so the contribution of solid solution strengthening was less than that of precipitation strengthening. Due to the fact that the grain size after annealing was about tens of microns, the contribution of grain boundary strengthening accounted for 13%. According to TEM results, the measured precipitates was based on the limited area, resulting in the volume fraction of precipitates underrated. Therefore, the contribution of precipitation strengthening may be underestimated and the calculated yield strength was lower than experimental strength. The contribution values of grain boundary strengthening were (37±3) and (42±11) MPa, respectively. And the calculated strength values of two alloys were (285±3) and (286±11) MPa, respectively. The calculated strength was at the same level with the experimental yield strength.

3.4 Corrosion behavior

Figure 10 shows the SEM images of two investigated alloys after IGC test. The results showed that the IGC took place in two investigated alloys. The maximum intergranular corrosion depth values of 7N01-I alloy and 7N01-II alloy were 9 and 14 μm, respectively. The corrosion morphologies are shown in Fig. 11 after EXCO test. It was significantly different in corrosion morphology of two 7N01 alloys. There were long flakes in 7N01-I alloy and much shorter flakes in 7N01-II alloy. The difference of corrosion morphology was related to grain morphology in the outer surface of two 7N01 alloys.

The GBPs and PFZ were more sensitive to the corrosion behavior than the inner-grain precipitates. The potential difference between GBPs and matrix resulted in the anodic dissolution of GBPs [18,33−36]. In particular, continuous GBPs provided more anode channel for IGC [37,38]. The

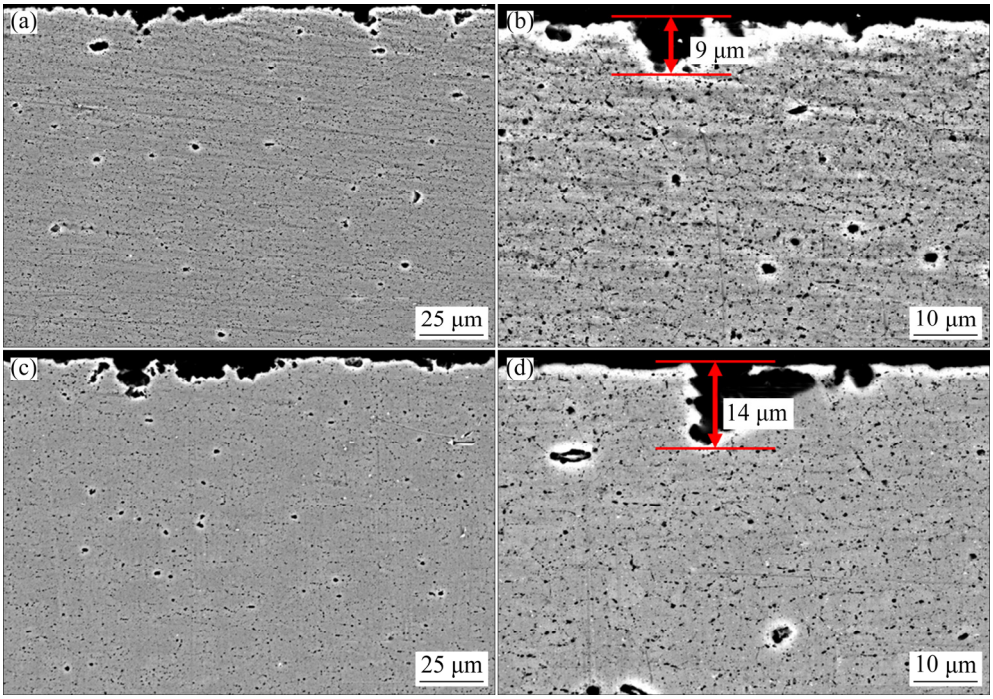

Fig. 10 SEM images of cross-section (in transverse section) of two 7N01 alloys after ICG test: (a, b) 7N01-I; (c, d) 7N01-II

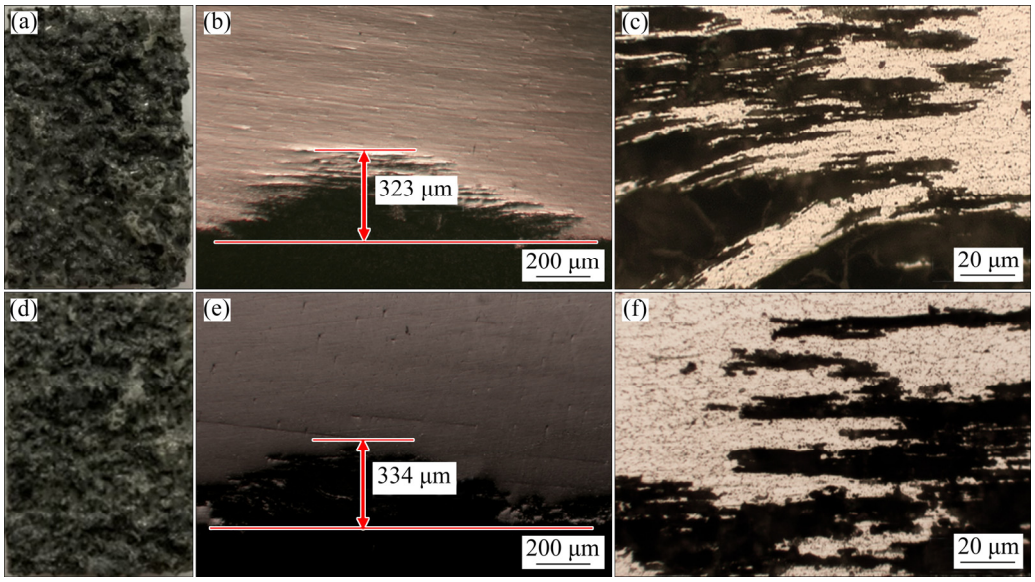

Fig. 11 Visual micrographs (a, d) and optical micrographs (b, c, e, f) in transverse section of two 7N01 alloys after EXCO test: (a−c) 7N01-I; (d−f) 7N01-II

recrystallized grain boundary had higher energy than sub-boundaries and η phase precipitated preferentially at high angle grain boundaries. The continuous η phase along high angle grain boundary was preferentially corroded. Once being formed, the crack propagated rapidly along grain boundary. The strength of the PFZ was much lower than that of the matrix. When the crack was formed, the wider PFZ also accelerated crack propagation [39−41].

The EXCO was usually originated from local intergranular corrosion. Precipitates on grain boundaries were corroded in EXCO test and intergranular corrosion cracks were formed. There were fibrous grains in alloys. The corrosion products in aqueous solution were beneficial to the lifting of uncorroded grain. When the corrosion cracks were formed, the cracks tended to propagate along the grain boundaries of the fibrous grains, and the corrosion products promoted the lifting of the uncorroded grains.

The difference of intergranular corrosion behavior of two 7N01 alloys was mainly due to the difference of GBPs and PFZ. The schematic diagram of corrosion behavior of two 7N01 alloys in longitudinal section is shown in Fig. 12. The continuous coarse GBPs of 7N01-II alloy provided more corrosion sites for the IGC and facilitated crack propagation. Compared with 7N01-II alloy, continuous GBPs in 7N01-I alloy were prone to the IGC resistance. The width of softer PFZ was also an important factor affecting corrosion propagation. The wide PFZ of 7N01-II alloy was conducive to crack propagation when the crack occurred.

The recrystallization degree was another factor affecting the corrosion behavior of two alloys. The crystallization degree of the outer surface of 7N01-I alloy was lower than that of 7N01-II alloy. There were more high-angle grain boundaries in the outer surface of 7N01-II alloy than that of 7N01-I alloy. The coarse precipitates at high angle grain boundaries promoted the susceptibility to IGC, so the IGC was more likely to occur in 7N01-II alloy. There were more stretched grains on the outer surface of 7N01-I alloy, which were more sensitive to EXCO, so more long flakes existed in 7N01-I alloy after the EXCO test.

4 Conclusions

(1) The grain morphology and recrystallization degree of 7N01-I alloy were similar to those of 7N01-II alloy. However, the recrystallization degree of the outer surface of 7N01-I alloy was lower than that of 7N01-II alloy. Fine η' phase uniformly distributed in the matrix of two 7N01 alloys. The GBPs of 7N01-I alloy distributed discontinuously, while those of 7N01-II alloy distributed continuously. The width of PFZ in 7N01-I alloy was slightly less than that of 7N01-II alloy.

(2) The YS, UTS and elongation of two 7N01 alloys were similar. And calculated yield strength was in good agreement with the experimental yield strength. The intergranular corrosion behavior of 7N01-I alloy was better than that of 7N01-II alloy because of discontinuous GBPs, narrower PFZ and lower crystallization degree of the outer surface of

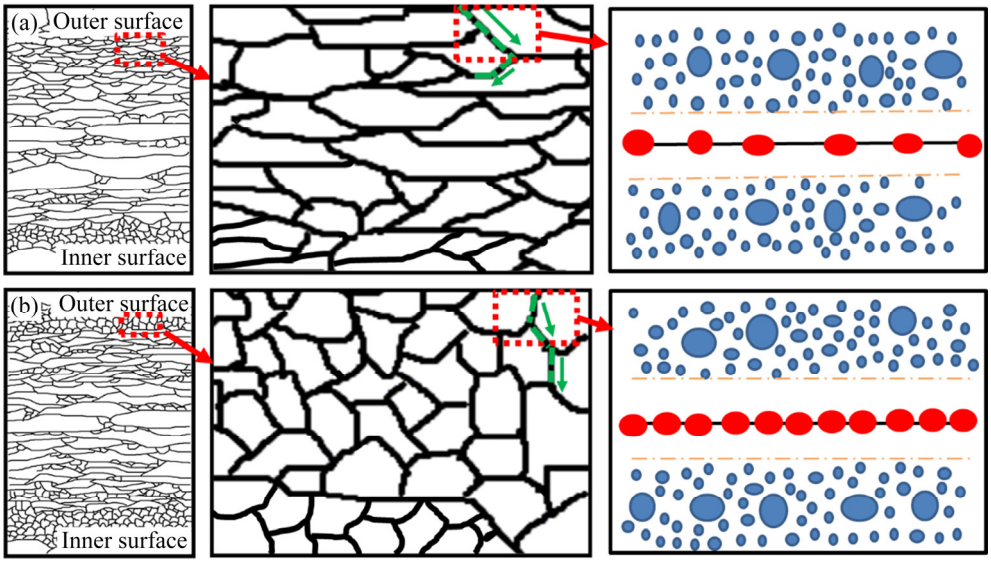

Fig. 12 Schematic diagram of corrosion behavior of two 7N01 alloys in longitudinal section: (a) 7N01-I; (b) 7N01-II

7N01-I alloy. There were more long flakes in 7N01-I alloy after EXCO test because the crystallization degree of the outer surface of 7N01-I alloy was lower than that of 7N01-II alloy.

Acknowledgments

The authors are grateful to the National Key Research and Development Program of China (Nos. 2021YFB3704204, 2021YFB3700902, 2021YFB3704205), Beijing Natural Science Foundation, China (No. 2202009), the National Natural Science Foundation of China (No. 51621003), Basic Research Program of Jiangsu Province (Natural Science Foundation), China (No. BK20191148), and Beijing Lab Project for Modern Transportation Metallic Materials and Processing Technology and Jiangsu Key Laboratory for Clad Materials, China (No. BM2014006).

References

[1] WILLIAMS J C, STARKE E A J. Progress in structural materials for aerospace systems [J]. Acta Materialia, 2003, 51: 5775−5799.

[2] HEINZ A, HASZLER A, KEIDEL C, MOLDENHAUER S, BENEDICTUS R, MILLER W S. Recent development in aluminum alloys for aerospace applications [J]. Materials Science and Engineering A, 2000, 280: 102−107.

[3] PENG Y H, LIU C Y, WEI L L, JIANG H J, GE Z J. Quench sensitivity and microstructures of high-Zn-content Al−Zn−Mg−Cu alloys with different Cu contents and Sc addition [J]. Transactions of Nonferrous Metals Society of China, 2021, 31: 24−35.

[4] XIAO Q F, HUANG J W, JIANG Y G, JIANG F Q, WU Y F, XU G F. Effects of minor Sc and Zr additions on mechanical properties and microstructure evolution of Al−Zn−Mg−Cu alloys [J]. Transactions of Nonferrous Metals Society of China, 2020, 30: 1429−1438.

[5] LIU J, YAO P, ZHAO N Q, SHI C S, LI H J, LI X, XI D S, YANG S. Effect of minor Sc and Zr on recrystallization behavior and mechanical properties of novel Al−Zn−Mg−Cu alloys [J]. Journal of Alloys and Compounds, 2016, 657: 717−725.

[6] WU H, WEN S P, HUANG H, LI B L, WU X L, GAO K Y, WNG W, NIE Z R. Effects of homogenization on precipitation of Al_3(Er,Zr) particles and recrystallization behavior in a new type Al−Zn−Mg−Er−Zr alloy [J]. Materials Science and Engineering A, 2017, 689: 313−322.

[7] WU H, WEN S P, LU J T, MI Z P, ZENG X L, HUANG H, NIE Z R. Microstructural evolution of new type Al–Zn–Mg–Cu alloy with Er and Zr additions during homogenization [J]. Transactions of Nonferrous Metals Society of China, 2017, 27: 1476−1482.

[8] LI X Z, HANSEN V, GJØNNESA J, WALLENBERG L R. HREM study and structure modeling of the η' phase, the hardening precipitates in commercial Al−Zn−Mg alloys [J]. Acta Materialia, 1999, 47: 2651−2659.

[9] PAULISCH M C, WANDERKA N, HAUPT M, SELVE S, DRIEHORST I, REIMERS W. The influence of heat treatments on the microstructure and the mechanical properties in commercial 7020 alloys [J]. Materials Science and Engineering A, 2015, 626: 254−262.

[10] PANSERI C, FEDERIGHI T. Evidence for the interaction between Mg atoms and vacancies in Al−Zn10%−Mg0.1% alloy [J]. Acta Metallurgica, 1963, 11: 575−584.

[11] DUMONT M, LEFEBVRE W, DOISNEAU B, DESCHAMPS A. Characterisation of the composition and volume fraction of η' and η precipitates in an Al−Zn−Mg alloy by a combination of atom probe, small-angle X-ray scattering and transmission electron microscopy [J]. Acta Materialia, 2005, 53: 2881−2892.

[12] XIE P, CHEN S Y, CHEN K H, JIAO H B, HUANG L P, ZHANG Z, YANG Z. Enhancing the stress corrosion cracking resistance of a low-Cu containing Al−Zn−Mg−Cu aluminum alloy by step-quench and aging heat treatment [J]. Corrosion Science, 2019, 161: 108184.

[13] MARLAUD T, DESCHAMPS A, BLEY F, LEFEBVRE W, BAROUX B. Evolution of precipitate microstructures during the retrogression and re-ageing heat treatment of an Al−Zn−Mg−Cu alloy [J]. Acta Materialia, 2010, 58: 4814−4826.

[14] ROUT P K, GHOSH M M, GHOSH K S. Microstructural, mechanical and electrochemical behavior of a 7017 Al−Zn−Mg alloy of different tempers [J]. Materials Characterization, 2015, 104: 49−60.

[15] LI B, WANG X M, CHEN H, HU J, HUANG C, GOU G Q. Influence of heat treatment on the strength and fracture toughness of 7N01 aluminum alloy [J]. Journal of Alloys and Compounds, 2016, 678: 160−166.

[16] MAHMOUD C, MAHMOUD K, KAROL J, GÉRARD M, ABDELWAHEB K. Characterization of the mechanical properties changes in an Al−Zn−Mg alloy after a two-step ageing treatment at 70 and 135 °C [J]. Materials & Design, 2010, 31: 3134−3139.

[17] PUIGGALI M, ZIELINSKI A, OLIVE J M, RENAULD E, DESJARDINS D, CID M. Effect of microstructure on stress corrosion cracking of an Al−Zn−Mg−Cu alloy [J]. Corrosion Science, 1998, 40: 805−819.

[18] KNIGHT S P, BIRBILIS N, MUDDLE B C, TRUEMAN A R, LYNCH S P. Correlations between intergranular stress corrosion cracking, grain-boundary microchemistry, and grain-boundary electrochemistry for Al−Zn−Mg−Cu alloys [J]. Corrosion Science, 2010, 52: 4073−4080.

[19] LI H, ZHAO P P, WANG Z X, MAO Q Z, FANG B J, SONG R G, ZHENG Z Q. The intergranular corrosion susceptibility of a heavily overaged Al−Mg−Si−Cu alloy [J]. Corrosion Science, 2016, 107: 113−122.

[20] SHU W X, HOU L G, ZHANG C, ZHANG F, LIU J C, LIU J T, ZHUANG L Z, ZHANG J S. Tailored Mg and Cu contents affecting the microstructures and mechanical properties of high-strength Al−Zn−Mg−Cu alloys [J]. Materials Science and Engineering A, 2016, 657: 269−283.

[21] DONG P X, CHEN S Y, CHEN K H. Effects of Cu content on microstructure and properties of super-high-strength Al−9.3Zn−2.4Mg−xCu−Zr alloy [J]. Journal of Alloys and Compounds, 2019, 788: 329−337.

[22] JIAO H B, CHEN K H, CHEN S Y, YANG Z, XIE P, CHEN S D. Effect of Cu on the fracture and exfoliation corrosion behavior of Al−Zn−Mg−*x*Cu alloy [J]. Metals, 2018, 8: 1048.
[23] STARINK M J, WANG P, SINCLAIR I, GREGSON P J. Microstructure and strengthening of Al−Li−Cu−Mg alloys and MMCs: I. Analysis and modelling of microstructural changes [J]. Acta Materialia, 1999, 47: 3841−3853.
[24] LÜTJERING G, ALBRECHT J, SAUER C, KRULL T. The influence of soft, precipitate-free zones at grain boundaries in Ti and Al alloys on their fatigue and fracture behavior [J]. Materials Science and Engineering A, 2007, 468: 201−209.
[25] ABE M, ASANO K, FUJIWARA A. Influence of the precipitate-free zone width on the tensile properties of an Al−6wt.%Zn−1.2wt.%Mg alloy [J]. Metallurgical and Materials Transactions B, 1973, 4: 1499−1505.
[26] GB/T 7998—2005. Test method for inter-granular corrosion of aluminum alloys [S]. 2005.
[27] GB/T 22639—2008. Test method of exfoliation corrosion for wrought aluminum and aluminum alloys [S]. 2008.
[28] HALL E O. The deformation and ageing of mild steel: III. Discussion of results [J]. Proceedings of the Royal Society of London, 1951, 643: 747−752.
[29] DESCHAMPS A, BRECHET Y. Influence of pre-deformation and aging of an Al−Zn−Mg alloy—II. Modeling of precipitation kinetics and yield stress [J]. Acta Materialia, 1998, 47: 293−305.
[30] DIXIT M, MISHRA R S, SANKARAN K K. Structure–property correlations in Al 7050 and Al 7055 high-strength aluminum alloys [J]. Materials Science and Engineering A, 2007, 478: 163−172.
[31] LABUSCH R. A Statistical theory of solid solution hardening [J]. Physica Status Solidi, 1970, 41: 659−669.
[32] GHIAASIAAN R, SHANKAR S. Structure−property models in Al−Zn−Mg−Cu alloys: A critical experimental *T* assessment of shape castings [J]. Materials Science and Engineering A, 2018, 733: 235−245.
[33] HUANG L P, CHEN K H, LI S, SONG M. Influence of high-temperature pre-precipitation on local corrosion behaviors of Al−Zn−Mg alloy [J]. Scripta Materialia, 2007, 56: 305−308.
[34] MARLAUD T, MALKI B, HENON C, DESCHAMPS A, BAROUX B. Relationship between alloy composition, microstructure and exfoliation corrosion in Al−Zn−Mg−Cu alloys [J]. Corrosion Science, 2011, 53: 3139−3149.
[35] LIU S D, CHEN B, LI C B, DAI Y, DENG Y L, ZHANG X M. Mechanism of low exfoliation corrosion resistance due to slow quenching in high strength aluminum alloy [J]. Corrosion Science, 2015, 91: 203−212.
[36] YUAN D L, CHEN K H, CHEN S Y, ZHOU L, CHANG J Y, HUANG L P, YI Y P. Enhancing stress corrosion cracking resistance of low Cu-containing Al−Zn−Mg−Cu alloys by slow quench rate [J]. Materials & Design, 2018, 164: 107558.
[37] XIAO Y P, PAN Q L, LI W B, LIU X Y, HE Y B. Influence of retrogression and aging treatment on corrosion behavior of an Al−Zn−Mg−Cu alloy [J]. Materials & Design, 2011, 32: 2149−2156.
[38] DENG Y, YIN Z M, ZHAO K, DUAN J Q, HU J, HE Z B. Effects of Sc and Zr microalloying additions and aging time at 120 °C on the corrosion behavior of an Al−Zn−Mg alloy [J]. Corrosion Science, 2012, 65: 288−298.
[39] MINODA T, YOSHIDA H. Effect of grain characteristic on intergranular corrosion resistance of 6061 aluminum alloy extrusion [J]. Metallurgical and Materials Transactions A, 2002, 33: 2891−2898.
[40] KIM S H, ERB U, AUST K T, PALUMBO G. Grain boundary character distribution and intergranular corrosion behavior in high purity aluminum [J]. Scripta Materialia, 2001, 44: 835−839.
[41] TSAI T C, CHUANG T H. Role of grain size on the stress corrosion cracking of 7475 aluminum alloys [J]. Materials Science and Engineering A, 1997, 225: 135−144.

工业 7N01 合金的显微组织、力学性能及腐蚀性能

赵沛浩[1]，吴晓蓝[1]，刘 阳[1]，高坤元[1]，文胜平[1]，魏 午[1]，
荣 莉[1]，黄 晖[1]，吴 宏[2]，周德敬[3]，张 倩[4]，聂祚仁[1]

1. 北京工业大学 材料与制造学部，北京 100124；2. 中南大学 粉末冶金国家重点实验室，长沙 410083；
3. 银邦金属复合材料股份有限公司 江苏省复合材料重点实验室，无锡 214145；
4. 中国铁道科学研究院集团有限公司 金属及化学研究所，北京 100081

摘 要：通过透射电子显微镜(TEM)和配备电子背散射衍射(EBSD)的扫描电子显微镜(SEM)研究晶粒形貌和析出相对两种工业 7N01 合金的力学性能和腐蚀行为的影响。7N01-I 合金外表面再结晶度低于 7N01-II 合金。两种合金的强化相均为 η'相。7N01-I 合金的晶界析出相(GBPs)断续分布，而 7N01-II 合金的晶界析出相连续分布。两种合金的强度接近，但 7N01-I 合金的最大腐蚀深度小于 7N01-II 合金，这是因为 7N01-I 合金外表面的低再结晶度和断续的 GBPs 有利于提高耐蚀性。讨论不同的强化机制，并分析显微组织与腐蚀行为的相关性。

关键词：7N01 合金；显微组织；力学性能；腐蚀行为

(Edited by Bing YANG)